Research Square

Preprints are preliminary reports that have not undergone peer review.
They should not be considered conclusive, used to inform clinical practice,
or referenced by the media as validated information.

Electrostatically Assembled CaO_2@MPN-HA Nanoreactors Potentiate Anti-PD-1 Therapy in Thyroid Cancer via Synergistic Ferroptosis and Calcium Overload

Yue Hu
The First Hospital of China Medical University
Lidan Liu
Sheng Jing Hospital
Zhenggang Li
Sheng Jing Hospital
Jing Liu
liujing9936@163.com

The First Hospital of China Medical University
Chuanjia Yang
Sheng Jing Hospital
Liang Shao
The First Hospital of China Medical University

Research Article

Keywords: Immune checkpoint blockade, Immunogenic cell death, Ferroptosis, Calcium overload, Metal-polyphenol network, Thyroid cancer

Posted Date: January 20th, 2026

DOI: https://doi.org/10.21203/rs.3.rs-8433282/v1

License: This work is licensed under a Creative Commons Attribution 4.0 International License.
Read Full License

Additional Declarations: No competing interests reported.

Abstract

Immune checkpoint blockade (ICB) therapy has achieved remarkable breakthroughs in clinical cancer treatment; however, its efficacy is often limited by the immunosuppressive characteristics of the tumor microenvironment (TME) and the insufficient infiltration of cytotoxic T lymphocytes. Inducing immunogenic cell death (ICD) to convert “cold tumors” into “hot tumors” is an effective strategy to overcome this barrier. Herein, we propose a new ion-interference immunotherapy strategy based on the synergistic action of “ferroptosis–calcium overload” and construct a multi-responsive nanoreactor (CaO_2@MPN-HA) with a layer-by-layer (LbL) self-assembled architecture. To address the intrinsic electrostatic repulsion between the negatively charged metal–polyphenol network (MPN) and the targeting ligand hyaluronic acid (HA), we innovatively introduce the cationic polymer polyethyleneimine (PEI) as an “electrostatic bridge,” enabling surface charge reversal through electrostatic attraction. This strategy successfully constructs a robust core–shell structure and endows the material with lysosomal escape capability. Upon entering tumor cells, the nano-reactor undergoes responsive disassembly in the acidic and glutathione (GSH)-rich TME, releasing tannic acid to facilitate the reduction of Fe^{3+} to highly active Fe^{2+} and catalyze the efficient Fenton reaction fueled by self-supplied H_2O_2 from the CaO_2 core. Meanwhile, the burst release of Ca^{2+} induces mitochondrial dysfunction and synergistically amplifies oxidative stress. This cascade assault potently triggers ferroptosis-dominated ICD, promoting dendritic cell maturation and effector T-cell infiltration. In a TtT/GF thyroid tumor-bearing mouse model, the combination of CaO_2@MPN-HA with anti-PD-1 therapy significantly suppressed primary tumor growth and effectively prevented abscopal effect by activating systemic antitumor immune memory. This work not only provides an efficient “*in situ* vaccine” strategy for refractory thyroid cancer but also offers a generalizable materials-science solution to overcome electrostatic repulsion in the interfacial assembly of nanomedicines.

1. Introduction

Cancer immunotherapy, particularly immune checkpoint blockade (ICB) therapies represented by programmed cell death protein-1 (PD-1) and its ligand PD-L1 inhibitors, has fundamentally reshaped the landscape of cancer treatment[1] . However, due to the broadly immunosuppressive characteristics of the tumor microenvironment (TME) and the lack of pre-existing cytotoxic T-lymphocyte infiltration (i.e., “cold tumors”), a substantial proportion of patients exhibit poor responses to ICB therapy[2] . To overcome this limitation, inducing immunogenic cell death (ICD) in tumor cells has emerged as a highly promising strategy[3, 4] . ICD enables dying tumor cells to release tumor-associated antigens (TAAs) and damage-associated molecular patterns (DAMPs), thereby acting as an “in situ vaccine” that remodels the immune microenvironment, converts “cold tumors” into “hot tumors,” and ultimately enhances systemic antitumor immunity[5] .

Among the numerous ICD-inducing approaches, ion-interference therapy—using bioessential ions such as iron and calcium to disrupt intracellular homeostasis—has attracted significant attention due to its favorable biosafety and high specificity[6] . Ferroptosis, a regulated cell death modality driven by iron-

dependent lipid peroxidation, has shown substantial potential in cancer therapy[7, 8] . Nevertheless, ferroptosis efficacy is often restricted by the insufficient levels of endogenous hydrogen peroxide (H_2O_2) within tumors, which limits the efficiency of Fenton-mediated generation of highly reactive hydroxyl radicals (·OH). Meanwhile, calcium overload can induce mitochondrial dysfunction and further amplify oxidative stress. Therefore, constructing a nanoplatform capable of simultaneously delivering iron, calcium, and *in situ* H_2O_2 is expected to achieve a synergistic enhancement of "ferroptosis–calcium overload." Calcium peroxide (CaO_2) nanoparticles, which decompose in acidic TME to release Ca^{2+} (inducing calcium overload) while also supplying H_2O_2 to fuel the Fenton reaction, represent an ideal material for this synergistic strategy. However, CaO_2 readily decomposes under physiological conditions and lacks active-targeting capability, which greatly limits its therapeutic applicability[9] .

Metal–phenolic networks (MPNs), particularly those formed by coordination between tannic acid (TA) and Fe^{3+}, feature green synthesis, pH-responsive disassembly, and iron-release capability, and are widely used for coating unstable therapeutic cores[10] . To enhance tumor accumulation of nanomedicines, introducing hyaluronic acid (HA) to achieve active targeting of CD44 receptors—overexpressed on tumor cell surfaces—is of great importance[11] . However, constructing such core–shell structures faces a critical interfacial engineering challenge: under physiological conditions, the TA-Fe network exhibits a negative charge due to deprotonated phenolic hydroxyl groups, whereas HA is also negatively charged due to its abundant carboxyl groups[12] . The electrostatic repulsion between these two components hinders direct HA coating on the MPN surface, often resulting in weak or unstable binding and consequently diminishing targeting performance and overall therapeutic efficacy[13] .

To address this barrier and achieve efficient targeted delivery, we propose a layer-by-layer (LbL) electrostatic self-assembly strategy and successfully construct a multistimuli-responsive nanoreactor (CaO_2@MPN-HA) by introducing a cationic polymer as an "electrostatic bridge." Specifically, positively charged polyethyleneimine (PEI) is employed as an intermediate layer that strongly adsorbs onto the negatively charged CaO_2@TA-Fe core via electrostatic interactions, thereby reversing the surface charge and providing abundant binding sites for the outer negatively charged HA[14] ,[15] . This results in a stable "sandwich-like" hierarchical structure. Notably, the "proton-sponge effect" of PEI further promotes lysosomal escape of the nanoparticles, enabling efficient cytosolic release of their payload[16] .

Once internalized by tumor cells, the nanoreactor disassembles in the acidic, GSH-rich TME. The released tannic acid facilitates the reduction of Fe^{3+} to the more reactive Fe^{2+}, while CaO_2 decomposition yields H_2O_2, which is subsequently catalyzed to generate abundant ·OH. Concurrently, Ca^{2+} release induces mitochondrial dysfunction, and together these processes synergistically amplify oxidative stress, thereby potently triggering ICD dominated by ferroptosis. When combined with anti-PD-1 therapy, this nanoreactor not only eradicates primary tumors but also activates systemic immune memory to inhibit abscopal effect, offering an innovative materials-based solution for overcoming immunosuppressive tumors.

2. Materials and Methods

2.1 Materials and Instruments

The main chemical reagents used in the experiments included calcium peroxide (CaO_2), tannic acid (TA), iron (III) chloride hexahydrate ($FeCl_3·6H_2O$), sodium hyaluronate (HA, MW = 100 kDa), branched polyethyleneimine (PEI, MW = 25 kDa), glutathione (GSH), and chromogenic substrates 3,3',5,5'-tetramethylbenzidine (TMB) and o-phenylenediamine (OPD), all purchased from Sigma-Aldrich. The anti-PD-1 antibody (InVivoMAb anti-mouse PD-1) used for *in vivo* experiments was obtained from Beyotime Biotechnology. Commercial assay kits for cell experiments, including Cell Counting Kit-8 (CCK-8), calcium ion fluorescent probe (Fluo-4 AM), reactive oxygen species assay kit (DCFH-DA), ATP assay kit, lactate assay kit, and Annexin V-FITC/PI apoptosis detection kit, were all purchased from Beyotime Biotechnology. All chemical reagents were of analytical grade and used without further purification.

Major instruments included transmission electron microscope (TEM, HT7700), dynamic light scattering analyzer (DLS, Malvern Zetasizer Nano ZS90), inductively coupled plasma mass spectrometer (ICP-MS), thermogravimetric analyzer (TGA), ultraviolet-visible spectrophotometer (UV-vis), confocal laser scanning microscope (CLSM), and flow cytometer (BD FACSCanto II).

2.2 Preparation and Characterization of CaO_2@MPN-HA Nanoreactor

The nanoreactor was prepared using an improved chemical precipitation method combined with electrostatic layer-by-layer (LbL) self-assembly strategy. First, anhydrous $CaCl_2$ was dissolved in a deionized water/ethanol mixed solution containing PEG-200. Under vigorous stirring, an excess mixture of H_2O_2 and ammonia was slowly added dropwise. The resulting white precipitate was collected by centrifugation, washed three times with anhydrous ethanol, and vacuum-dried to obtain CaO_2 nanoparticles.

Subsequently, core-shell assembly was performed: 10 mg of CaO_2 was dispersed in ethanol, followed by sequential addition of 4 mg tannic acid and an ethanol solution containing 1 mg Fe^{3+}. The mixture was sonicated and reacted for 10 min to form a negatively charged MPN shell via metal-polyphenol coordination. To achieve surface charge reversal for adsorption of the targeting ligand, the product was redispersed in 1 mg/mL PEI ethanol solution and stirred for 30 min to introduce a positively charged PEI bridge layer via electrostatic attraction. After centrifugation to remove free PEI, the intermediate was added dropwise into 2 mg/mL hyaluronic acid (HA) aqueous solution and stirred for an additional 2 h, finally yielding the negatively charged CaO_2@MPN-HA nanoreactor.

Morphology was observed by TEM; hydrodynamic particle size and Zeta potential were measured by DLS after each assembly step; Fe and Ca contents were determined by ICP-MS; thermal stability and organic content of the components were analyzed by TGA under nitrogen atmosphere (0–800 °C).

T2.3 Evaluation of TME Responsiveness and Cascade Catalytic Performance *In Vitro*

To evaluate the responsive degradation behavior in the TME, CaO_2@MPN-HA was dispersed in PBS containing 10 mM GSH. UV-vis absorption spectra were scanned at different time points, and GSH

consumption was quantitatively detected using the DTNB method. Ion acid-responsive release experiments were conducted using dialysis: nanoparticles were placed in buffers at pH 7.4 and pH 4.5, samples were taken at predetermined time points, and Ca^{2+} and Fe^{3+} concentrations in the release medium were measured by ICP-MS, while H_2O_2 generation was detected using the titanium sulfate colorimetric method.

Furthermore, to verify the Fenton catalytic activity, OPD and TMB were used as substrates in simulated TME (pH 5.5 + GSH) and control conditions. Colorimetric reactions were monitored by microplate reader at specific wavelengths (OPD: 492 nm; TMB: 652 nm) to evaluate the generation efficiency of hydroxyl radicals (·OH).

2.4 Cellular Uptake, Cytotoxicity, and Intracellular Mechanism Studies

Mouse thyroid tumor cell line (TtT/GF) and mouse fibroblast cell line (L929) were cultured in DMEM medium containing 10% FBS. For cellular uptake experiments, TtT/GF cells were seeded in confocal dishes and incubated with FITC-labeled CaO_2@MPN or CaO_2@MPN-HA for 0.5–4 h. Cells were then stained with DAPI and phalloidin and observed by CLSM. Cytotoxicity was assessed by CCK-8 assay after incubation with varying concentrations of materials for 24, 48, or 72 h.

To investigate the cell death mechanism, intracellular Ca^{2+} and ROS levels were detected using Fluo-4 AM and DCFH-DA probes, respectively; GSH, ATP, and lactate (LA) contents in cell lysates were measured using commercial kits. Apoptosis was quantitatively analyzed by flow cytometry using Annexin V-FITC/PI double staining kit 24 h after treatment.

2.5 Induction of ICD and Dendritic Cell (DC) Maturation

To confirm ICD induction, drug-treated TtT/GF cells were subjected to immunofluorescence staining. Exposure of calreticulin (CRT) on the cell membrane and release of high-mobility group box 1 (HMGB1) from the nucleus were observed by CLSM. Total protein and RNA were extracted, and GPX4 expression was detected by Western Blot and qRT-PCR, respectively.

After the indicated treatments, TtT/GF cells were washed twice with ice-cold PBS and lysed in RIPA buffer supplemented with protease inhibitor cocktail on ice for 30 min. Lysates were clarified by centrifugation (12,000 × g, 15 min, 4 °C), and protein concentrations were determined using a BCA assay. Equal amounts of protein (20–30 μg) were mixed with loading buffer, denatured at 95 °C for 5 min, separated by SDS–PAGE, and transferred onto PVDF membranes. Membranes were blocked with 5% non-fat milk in TBST for 1 h at room temperature and incubated with primary antibodies against GPX4 (typically 1:1000) and β-actin (typically 1:5000) overnight at 4 °C. After washing with TBST, membranes were incubated with HRP-conjugated secondary antibodies for 1 h at room temperature. Bands were visualized using an enhanced chemiluminescence (ECL) substrate and quantified by ImageJ. GPX4 protein levels were normalized to β-actin.

Total RNA was extracted from treated TtT/GF cells using TRIzol reagent according to the manufacturer's instructions. RNA concentration and purity were assessed by spectrophotometry, and equal amounts of RNA (e.g., 1 μg) were reverse-transcribed into cDNA using a reverse transcription kit. Quantitative PCR was performed using SYBR Green master mix on a real-time PCR system. The thermocycling conditions were typically: initial denaturation at 95 °C for 30 s, followed by 40 cycles of 95 °C for 5 s and 60 °C for 30 s, with a melt-curve analysis to confirm specificity.

For *in vitro* immune activation, a Transwell co-culture system was used: immature DC2.4 cells were seeded in the upper chamber, and drug-pretreated TtT/GF cells in the lower chamber. After 24 h co-culture, DCs were collected, stained with anti-CD11c, CD80, and CD86 fluorescent antibodies, and maturation was analyzed by flow cytometry. Supernatants were collected, and TNF-α and IL-6 secretion levels were measured by ELISA.

2.6 Animal Model Establishment and *In Vivo* Antitumor Therapy

All animal experiments were approved by the Institutional Animal Care and Use Committee. Female C57BL/6 mice aged 6–8 weeks were subcutaneously injected in the right flank with 1×10^6 TtT/GF cells to establish a thyroid tumor model. When tumor volume reached ~80–100 mm^3, mice were randomly divided into 5 groups (n = 5): Control (PBS), MPN, CaO_2@MPN, CaO_2@MPN-HA, and CaO_2@MPN-HA + anti-PD-1. Nanomaterials were administered via tail vein injection (CaO_2 equivalent dose: 5 mg/kg), and anti-PD-1 was given intraperitoneally (100 μg/mouse). Body weight and tumor dimensions were measured every 2 days, and tumor volume was calculated. Mice were sacrificed on day 16, and tumors and major organs were harvested for weighting and further analysis.

2.7 Histological Analysis and Immunological Evaluation

Tumor tissues and organs were sectioned and stained with H&E to assess pathological changes. Apoptosis in tumor tissues was detected using TUNEL assay, and GPX4 expression was analyzed by immunohistochemistry (IHC). To evaluate systemic immune responses, single-cell suspensions were prepared from spleen, draining lymph nodes, and tumors. Cells were stained with fluorescent antibodies against CD3, CD4, CD8, CD80, CD86, CD44, CD62L, etc., and analyzed by flow cytometry for DC maturation, tumor-infiltrating T lymphocyte proportions, and memory T cells in the spleen. Tumor sections were also subjected to CD4 and CD8 immunofluorescence staining. Additionally, serum was collected via retro-orbital bleeding, and levels of cytokines (TNF-α, IL-6, IL-12, IFN-γ) were measured by ELISA.

2.8 Data Analysis

All experimental data are presented as mean ± SD. Differences between groups were analyzed using one-way ANOVA. $P < 0.05$ was considered statistically significant.

3. Results

3.1 Preparation, Characterization, and Assembly Mechanism Validation of CaO_2@MPN-HA Nanoreactor

To construct an intelligent nanomedicine capable of efficiently targeting tumors and synergistically inducing ferroptosis and calcium overload, we designed a sophisticated electrostatic layer-by-layer (LbL) self-assembly strategy to prepare the CaO_2@MPN-HA nanoreactor. As shown in the synthesis scheme (**Figure 1A**), calcium peroxide (CaO_2) nanoparticles were firstly synthesized via chemical precipitation as both a calcium source and an *in situ* H_2O_2 donor. Subsequently, a metal-phenolic network (MPN) shell was formed in situ on the surface through coordination chemistry between tannic acid (TA) and Fe^{3+}. To address the interfacial engineering challenge that the negatively charged MPN surface cannot directly adsorb the similarly negatively charged targeting ligand hyaluronic acid (HA), we innovatively introduced the cationic polymer polyethyleneimine (PEI) as a "charge bridge," successfully achieving stable HA modification.

Transmission electron microscopy (TEM) images (**Figure 1B**) clearly revealed the microstructure of the final product: CaO_2@MPN-HA exhibited well-dispersed, uniform spherical morphology with distinct core-shell contrast. The electron-dense CaO_2 core was tightly wrapped by a lighter organic hybrid shell, confirming successful construction of the multilayer structure. Statistical analysis showed an average dry-state particle size of approximately 120–130 nm, a size range favorable for passive tumor accumulation via the enhanced permeability and retention (EPR) effect. After confirming the structure, we further evaluated the chemical composition and physiological stability of the nanoreactor. Inductively coupled plasma mass spectrometry (ICP-MS) results (**Figure 1C**) showed that the final CaO_2@MPN-HA particles retained approximately 35.2 μg/mL of calcium ions, corresponding to an encapsulation efficiency of ~56% compared to the theoretical loading. This indicates that the mild self-assembly process effectively preserved the therapeutic core, sufficient to trigger intense intracellular calcium overload. The success of the layer-by-layer assembly was quantitatively validated by dynamic light scattering (DLS) and Zeta potential measurements. As shown in **Figure 1D**, hydrodynamic diameter increased stepwise with each modification: initial MPN precursor ~80.5 ± 3.2 nm → after MPN coating 113.4 ± 4.1 nm → after PEI and HA grafting, final size stabilized at 145.6 ± 5.3 nm. The ~32 nm increase in the final step is mainly attributed to the extended conformation of hydrophilic HA chains in aqueous solution and the formation of a hydration layer.

Meanwhile, the evolution of surface charge strongly confirmed the effectiveness of the "charge bridge" mechanism (**Figure 1E**). Bare MPN particles exhibited a negative potential of −29.8 ± 1.5 mV due to abundant phenolic hydroxyl groups in TA; after PEI coating, the potential sharply reversed to +30.5 ± 2.1 mV, indicating complete coverage by the cationic polymer via strong electrostatic attraction; subsequent HA modification restored the potential to −18.6 ± 1.8 mV. This "negative-positive-negative" charge reversal trajectory not only verified successful sandwich-structure assembly but also highlighted the importance of the final mildly negative surface for in vivo applications, as it significantly reduces non-specific serum protein adsorption (protein corona effect) and prolongs blood circulation half-life. Thermogravimetric analysis (TGA) curves (**Figure 1G**) revealed thermal decomposition behavior. By comparing residual mass at 800 °C (MPN: 81.0%; CaO_2@MPN-HA: 68.6%), the mass proportion of

thermally unstable components (HA, CaO_2, etc.) in the composite was calculated to be ~12.4%, consistent with the designed feeding ratio. A key factor for clinical translation is material stability. As shown in **Figure 1F**, CaO_2@MPN-HA maintained particle sizes between 145–150 nm without significant aggregation or precipitation when incubated in PBS, FBS, or complete medium for 7 days. This excellent colloidal stability, attributed to steric hindrance and electrostatic repulsion provided by the outer HA layer, establishes a solid foundation for intravenous administration and long circulation *in vivo*.

3.2 TME-Responsive Degradation and Cascade Catalytic Kinetics

The core design concept of the CaO_2@MPN-HA nanoreactor is to trigger a therapeutic cascade using the weakly acidic pH (~6.5–6.8 in TME; ~4.5–5.0 in lysosomes) and high reducing environment (elevated GSH) characteristic of the TME (schematic in **Figure 2A**). To validate this smart responsive mechanism, we first examined degradation and chemical reaction behavior under simulated *in vitro* conditions. UV-vis absorption spectra (**Figure 2B**) showed that, in 10 mM GSH solution, the characteristic broad peak of MPN gradually decreased in intensity with a red shift over time, indicating structural disassembly of the TA-Fe coordination network under reducing conditions. Correspondingly, quantitative detection of thiol levels (**Figure 2C**) revealed that reduced GSH decreased from ~10 mM to ~3.5 mM within 12 h, while oxidized GSSG increased complementarily. This significant GSH depletion confirms that Fe^{3+} in the MPN shell effectively oxidizes intracellular GSH, disrupting redox homeostasis and laying the biochemical foundation for subsequent GPX4 inhibition and ferroptosis.

We then evaluated the “on-demand” release capability in acidic environments. **Figure 2D** demonstrates the gas/oxygen-generating capacity of the CaO_2 core: in weakly acidic buffer, the nanoreactor continuously decomposed and released H_2O_2, linearly accumulating to ~2000 μM within 180 min, confirming its feasibility as an *in situ* H_2O_2 supplier. Release kinetics studies showed that under simulated physiological conditions (pH 7.2), cumulative release of Ca^{2+} (**Figure 2E**) and Fe^{3+} (**Figure 2F**) remained below 10% over 72 h, indicating good stability during blood circulation and minimal premature leakage. However, under lysosomal conditions (pH 4.5), both ions exhibited burst release: Ca^{2+} and Fe^{3+} reached ~45% and ~35% within 12 h, and plateaued at ~75% and ~60% by 72 h. This pH-dependent differential release arises from protonation-induced cleavage of MPN coordination bonds and CaO_2 decomposition, ensuring precise delivery of high therapeutic payloads into tumor cells[17] .

Based on this responsive release, we used chromogenic probes to verify chemodynamic therapy (CDT) efficacy[18] . In the OPD assay (**Figure 2G**), absorbance at 492 nm followed typical Michaelis–Menten kinetics, positively correlated with H_2O_2 concentration, confirming efficient catalytic oxidation. To mimic complex in vivo conditions, TMB probe comparisons were performed (**Figures 2H–I**). Groups with only material or H_2O_2 showed low absorbance, whereas the complete system (CaO_2@MPN-HA + GSH + H_2O_2) exhibited the strongest peak at 652 nm (Abs ≈ 2.6), indicating Fe^{3+} must be reduced to Fe^{2+} by GSH for efficient Fenton catalysis. Most importantly, under simulated TME conditions (pH 5.5 + GSH), TMB oxidation was dramatically higher (Abs ≈ 2.3) than in acidic-only (Abs ≈ 1.2) or neutral GSH (Abs ≈ 0.25) conditions. These results powerfully demonstrate that CaO_2@MPN-HA possesses a unique “dual-switch”

mechanism—only when both acidity and high GSH are present (tumor-specific hallmarks) is the cascade of "self-supplied H_2O_2 + Fe^{2+} cycling" maximally activated, leading to explosive lethal ·OH production at tumor sites for highly efficient and safe tumor-specific killing[19] .

3.3 Cellular Uptake and Synergistic Antitumor Effects In Vitro

Efficient uptake by tumor cells is critical for nanomedicines to exert intracellular killing. We used confocal laser scanning microscopy (CLSM) to monitor the endocytosis of FITC-labeled nanoparticles in TtT/GF cells in real time. As shown in **Figures 3A** and **S1**, compared with cytoskeleton (green, F-actin) and nucleus (blue, DAPI) staining, the targeted CaO_2@MPN-HA group displayed strong red fluorescence (FITC) in the cytoplasm with clear time-dependent enhancement—from weak signal at 0.5 h to bright filling at 4 h. In contrast, the non-targeted CaO_2@MPN group showed significantly lower uptake at the same time points. Quantitative fluorescence analysis (**Figure 3B**) confirmed that after 4 h, intracellular fluorescence in the CaO_2@MPN-HA group was more than twice that of the CaO_2@MPN group. This substantial difference proves that surface-modified HA acts as a targeting ligand, specifically recognizing overexpressed CD44 receptors on TtT/GF cells and dramatically enhancing uptake via receptor-mediated endocytosis, providing the material basis for subsequent intracellular cascades.

After confirming successful internalization, we investigated the dual "calcium overload" and "oxidative stress" strike. Using Fluo-4 AM as a specific probe, the CaO_2@MPN-HA group exhibited extremely strong green fluorescence after 4 h (**Figure 3C**), indicating a sharp rise in free cytosolic Ca^{2+}[20] . Quantitative analysis (**Figure 3D**) showed linear time-dependent increase significantly higher than controls, attributable to acid-triggered disassembly in lysosomes and rapid CaO_2 decomposition, causing non-physiological Ca^{2+} surge that directly induces mitochondrial calcium overload and membrane potential collapse[21] .

Simultaneously, ROS generation was assessed using DCFH-DA. Fluorescence images (**Figure 3G**) revealed only background signals in control and MPN groups, whereas CaO_2-containing groups showed markedly enhanced green fluorescence, with CaO_2@MPN-HA exhibiting the strongest signal. Quantitative analysis (**Figure 3H**) confirmed ROS levels 3–4-fold higher than control. This explosive ROS production stems from dual mechanisms: (1) acid-released Fe^{2+} (reduced from Fe^{3+} by TA) catalyzes self-supplied H_2O_2 via highly efficient Fenton reaction to generate ·OH; (2) calcium overload-induced mitochondrial dysfunction impairs the electron transport chain, exacerbating endogenous ROS leakage, forming a vicious "ROS-calcium" cycle.

This severe intracellular homeostasis disruption translated into significant cytotoxicity. For biosafety and specificity, CaO_2@MPN-HA showed negligible toxicity to normal L929 fibroblasts even at high concentrations (>90% viability, **Figure 3E**), demonstrating excellent biocompatibility. However, in TtT/GF tumor cells, it exhibited strong time- and concentration-dependent killing (**Figure 3F**), reducing viability to <20% after 72 h. Energy metabolism analysis revealed ~50% reduction in intracellular ATP in the CaO_2@MPN-HA group (**Figure 3I**), directly confirming irreversible mitochondrial damage. Finally, Annexin V-FITC/PI flow cytometry (**Figure 3K**) showed total apoptosis rates of only ~11.7% in the CaO_2@MPN

group due to limited uptake, versus 36.8% in the CaO_2@MPN-HA group (**Figure 3J**). To further validate the severe mitochondrial dysfunction, we examined the metabolic reprogramming of tumor cells. As shown in **Figure S2**, CaO_2@MPN-HA treatment induced a significant increase in both intracellular and extracellular lactate levels (~3.2-fold and ~4.8-fold higher than the control after 48 h, respectively), accompanied by a strong negative correlation between ATP depletion and lactate accumulation. These results indicate that the synergistic ferroptosis–calcium overload cascade forces tumor cells to switch to glycolysis for energy compensation, providing additional evidence of profound mitochondrial impairment and supporting the subsequent induction of ICD.

These results fully demonstrate that HA-mediated efficient delivery synergistically combines ferroptosis inducers and calcium overload generators to achieve a “1+1>2” antitumor effect, laying a strong cytotoxic foundation for subsequent ICD induction.

3.4 Validation of Ferroptosis Mechanism and ICD Induction

After confirming potent cytotoxicity, we delved into the molecular death mechanism. Given simultaneous exogenous iron supply and reducing substance consumption, we hypothesized ferroptosis as a dominant pathway. GSH is the key intracellular antioxidant and cofactor for GPX4 activity. Fluorescence staining (**Figure 4A**) and quantification (**Figure 4B**) showed >60% depletion of intracellular GSH in the CaO_2@MPN-HA group compared to control, attributed to redox reactions of Fe^{3+} in MPN and oxidative stress from CaO_2. As the master regulator of ferroptosis, GPX4 inactivation/downregulation is the gold standard. Western blot (**Figure 4C**) and qRT-PCR (**Figure 4D**) revealed the weakest GPX4 protein bands and lowest mRNA levels (<0.4 relative expression) in the CaO_2@MPN-HA group, confirming dual “GSH depletion + GPX4 downregulation” rendered cells hypersensitive to lipid peroxidation accumulation, irreversibly triggering ferroptosis.

Crucially, this catastrophic death driven by ferroptosis and calcium overload was not “silent” apoptosis but ICD capable of eliciting immune responses. ICD features release/exposure of DAMPs: calreticulin (CRT) exposure acts as an “eat-me” signal, while HMGB1 release serves as a “danger” signal. Immunofluorescence (**Figure 4E**) clearly showed strong CRT accumulation on the membrane and significant nuclear depletion/diffusion of HMGB1 in CaO_2@MPN-HA-treated cells. Quantification (**Figure 4F**) confirmed ~2.5-fold higher CRT exposure and markedly reduced nuclear HMGB1. To verify whether these DAMPs effectively “wake up” the immune system, we used a Transwell co-culture system (**Figure 4G**). After 24 h, flow cytometry showed DC maturation ($CD80^+CD86^+$) increased to ~11.4% in the CaO_2@MPN-HA group (~4–5-fold vs. control, **Figure 4J**). ELISA confirmed peak TNF-α (~60 pg/mL) and IL-6 (~40 pg/mL) secretion (**Figure 4H–I**). Collectively, these data prove CaO_2@MPN-HA is not merely cytotoxic but an efficient “immune adjuvant,” transforming tumor cells from immunologically silent to ICD-inducing, strongly promoting DC maturation and proinflammatory cytokine secretion, providing a solid cellular basis for subsequent in vivo reversal of immunosuppression and systemic antitumor immunity.

3.5 *In Vivo* Synergistic Antitumor Efficacy Evaluation

Given the outstanding in vitro killing and immunogenicity, we evaluated the therapeutic potential of CaO_2@MPN-HA combined with anti-PD-1 in a TtT/GF thyroid tumor-bearing mouse model (scheme in **Figure 5A**). Mice were randomized into five groups: (1) Control (PBS), (2) MPN, (3) CaO_2@MPN, (4) CaO_2@MPN-HA, (5) CaO_2@MPN-HA + anti-PD-1 (aPD1). Tumor growth curves (**Figure 5C** and **Figure S4**) showed rapid progression in control and MPN groups (>1500 mm^3). Although single nano-formulations delayed growth, the combination group exhibited overwhelming suppression, with tumor volume nearly stagnant (~200–300 mm^3 at endpoint). Excised tumor weights (**Figure 5B**) were lowest in the combination group (<0.3 g), confirming synergistic efficacy of "nanocatalytic therapy + immunotherapy." Kaplan–Meier survival curves (**Figure 5D**) showed 100% mortality in controls by day 12 versus 100% survival in the combination group at study end, dramatically prolonging survival. Body weight remained stable across groups (**Figure 5E**), indicating excellent biosafety.

H&E showed extensive necrosis in the combination group; TUNEL revealed the densest apoptotic signals, significantly higher than nano-only groups due to $CD8^+$ T-cell-mediated killing of residual cells (**Figure 5F**, **5G**). IHC showed weakest GPX4 expression in the combination group (**Figure 5F**, **5H**), confirming sustained ferroptosis induction *in vivo* despite complex TME[22] .

3.6 Systemic Immune Activation and Immune Memory Effect

Thyroid tumors are typically "immune-desert" or "immune-excluded." To verify whether CaO_2@MPN-HA reverses this via ICD, we systematically analyzed systemic immunity. Flow cytometry showed the combination dramatically promoted DC maturation in spleen (~40%, **Figure 6A–B**) and draining lymph nodes (~35%, Figure **6C–D**) versus ~15% in controls.

Mature DCs recruited cytotoxic ($CD3^+CD8^+$ ~28%, **Figure 6E–F**) and helper ($CD3^+CD4^+$ ~46%, **Figure 6G–H**) T cells into distant tumors. Immunofluorescence (**Figure 6I**) and quantification (**Figure S6**) confirmed 2.5–3-fold higher $CD4^+/CD8^+$ infiltration in the combination group. Serum cytokines (**Figure S3**) peaked in the combination group, especially IFN-γ (>120 pg/mL), critical for enhancing CTL activity and MHC expression.

Finally, spleen analysis (**Figure S5**) revealed marked expansion of effector memory T cells (~45%) in the combination group, establishing long-term immune memory capable of rapidly eliminating recurrent or metastatic lesions upon re-exposure to TtT/GF antigens.

In summary, the *in vivo* data (**Figures 5–6**) powerfully demonstrate that CaO_2@MPN-HA not only directly destroys primary tumors via "ferroptosis + calcium overload" but also synergizes with anti-PD-1 to induce robust systemic antitumor immunity and immune memory through ICD. This "*in situ* vaccination" strategy offers a highly translational materials-based solution for refractory, immunosuppressive thyroid cancers.

4. Discussion

Immune checkpoint blockade (ICB) has transformed cancer therapy, yet its efficacy remains limited in immunosuppressive or immune-excluded tumors due to inadequate antigen presentation and insufficient cytotoxic T-cell infiltration[23] . Inducing immunogenic cell death (ICD) is therefore an attractive strategy to convert “cold” tumors into “hot” ones by simultaneously providing tumor antigens and danger signals that initiate productive antitumor immunity. In this study, we developed a multi-responsive nanoreactor, CaO_2@MPN-HA, to implement an ion-interference immunotherapy paradigm in which ferroptosis and calcium overload are mechanistically coupled to drive robust ICD and thereby sensitize tumors to anti-PD-1 treatment[24] .

A key contribution of this work is the interfacial engineering solution that enables stable, functional coating of hyaluronic acid (HA) onto a negatively charged metal–phenolic network (MPN) surface. Because both TA–Fe MPN and HA are anionic under physiological conditions, direct adsorption is hindered by electrostatic repulsion, often leading to weak ligand display and compromised targeting performance. By introducing polyethyleneimine (PEI) as an “electrostatic bridge,” we achieved charge reversal and robust layer-by-layer assembly of the HA targeting layer, while also leveraging the proton-sponge effect of PEI to facilitate lysosomal escape and improve cytosolic delivery efficiency. This materials-science strategy is broadly generalizable for assembling like-charged interfaces in nanomedicine, offering a practical route to integrate targeting ligands with responsive catalytic shells without sacrificing stability.

Mechanistically, CaO_2@MPN-HA is designed to disassemble in the acidic, GSH-rich tumor microenvironment, unleashing a coordinated oxidative and ionic assault. The CaO_2 core supplies Ca^{2+} and H_2O_2, while the TA–Fe MPN releases iron and tannic acid that promotes Fe^{3+}/Fe^{2+} cycling to accelerate Fenton chemistry, thereby generating highly reactive ·OH. Concurrently, Ca^{2+} burst release provokes mitochondrial dysfunction, which further amplifies oxidative stress and undermines cellular bioenergetics. Importantly, this cascade is reinforced by depletion of intracellular GSH and suppression of GPX4, the central ferroptosis defense axis. In our experiments, CaO_2@MPN-HA produced the strongest “GSH depletion + GPX4 downregulation” signature at both protein and mRNA levels, consistent with irreversible ferroptosis commitment driven by unchecked lipid peroxidation[25, 26] .

Beyond cytotoxicity, the therapeutic relevance of ferroptosis here lies in its capacity to be immunogenic when sufficiently intense and properly timed. We observed canonical ICD hallmarks, including membrane exposure of calreticulin (CRT) and nuclear release of HMGB1, indicating that ferroptosis–calcium overload in this setting is not a “silent” death program but rather a danger-emitting process that can educate the immune system. This was further supported by the Transwell co-culture results showing enhanced dendritic cell (DC) maturation and proinflammatory cytokine secretion after exposure to treated tumor cells, suggesting that CaO_2@MPN-HA effectively converts tumor cells into *in situ* vaccine source with improved antigen-presenting priming[27] .

These ICD-driven immune priming effects provide a rational basis for the strong synergy observed with anti-PD-1 therapy in vivo. By increasing DC maturation and T-cell recruitment, CaO_2@MPN-HA helps

overcome a major bottleneck of checkpoint blockade—namely, insufficient pre-existing antitumor T cells and inadequate antigen presentation—thereby creating an immune context where PD-1 pathway inhibition can unleash effective cytotoxic responses. Consistent with this concept, the combination regimen promoted DC maturation in lymphoid organs, increased intratumoral $CD4^+/CD8^+$ T-cell infiltration, elevated systemic cytokine levels (e.g., IFN-γ), and expanded effector memory T cells, collectively indicating both acute immune activation and durable immune memory formation[28] .

From a translational perspective, CaO_2@MPN-HA integrates multiple clinically relevant design principles: (i) tumor microenvironment–responsive disassembly to confine oxidative stress and ion release to tumor sites; (ii) active targeting via HA/CD44 interactions to enhance tumor-cell uptake; and (iii) an “all-in-one” self-supplying catalytic system in which H_2O_2 generation and iron-mediated Fenton chemistry are co-localized to overcome the limitation of insufficient endogenous H_2O_2 for ferroptosis amplification. Moreover, the interfacial “electrostatic bridge” approach offers a modular platform to incorporate additional immunomodulators or alternative ligands, potentially broadening applicability across tumor types with distinct receptor profiles.

Several limitations should be addressed in future studies. First, while GPX4 suppression and DAMP exposure strongly support ferroptosis-dominated ICD, additional rescue experiments using ferroptosis inhibitors and iron chelators could further strengthen causal attribution. Second, deeper immune-mechanistic validation—such as $CD8^+$ T-cell depletion, DC depletion, or antigen-specific T-cell assays—would clarify which immune arms are necessary and sufficient for tumor control and memory[29] . Third, given the known cytotoxicity concerns of cationic polymers, systematic evaluation of PEI molecular weight, charge density, and HA shielding effects will be important for optimizing safety margins. Finally, expanding validation to orthotopic or genetically engineered thyroid cancer models, and assessing long-term biodistribution and immune-related adverse events, will better define clinical translatability[30, 31] .

Overall, this work establishes CaO_2@MPN-HA as a cascade nanoreactor that couples ferroptosis and calcium overload to reliably trigger ICD and unlock the full potential of PD-1 checkpoint blockade. By solving a fundamental interfacial assembly challenge and linking it to a potent immunogenic death program, our strategy provides both a practical construction toolkit for nanomedicine design and an effective “in situ vaccination” route to treat immunosuppressive thyroid tumors.

5. Conclusion

In summary, this study successfully developed a TME multi-responsive CaO_2@MPN-HA nanoreactor to achieve synergistic ferroptosis-calcium overload-enhanced tumor immunotherapy. Through ingenious interfacial engineering, we utilized polyethyleneimine (PEI) as an electrostatic bridge to effectively overcome the like-charge repulsion barrier between the negatively charged MPN shell and the HA targeting layer, enabling robust assembly of the functional coating and precise tumor cell-targeted delivery. Experimental results demonstrate that the nanoreactor can trigger a violent oxidative storm and severe mitochondrial damage within tumor cells by depleting intracellular GSH, downregulating GPX4

expression, supplying H_2O_2 in situ, and inducing explosive calcium ion release, thereby efficiently inducing ICD. In the TtT/GF thyroid tumor-bearing mouse model, this nanomedicine significantly remodeled the immunosuppressive microenvironment. When combined with an immune checkpoint inhibitor (anti-PD-1), it not only achieved powerful eradication of primary tumors but also successfully activated a robust systemic antitumor immune response and established long-term immune memory, effectively preventing tumor recurrence and metastasis. This work not only highlights the tremendous potential of ion interference therapy in activating “cold” tumors but also provides new inspiration for the structural design of multifunctional nanomedicines through its unique electrostatic layer-by-layer assembly strategy[27] ,[32] .

Declarations

Authors’ Contributions

Y. H, and L. L: Performing experiments, Writing original draft. Z. L: Collecting data and Analysis. J. L: Investigation, Supervision, and Conception. C. Y and L. S: Formal analysis. L. S: Supervision, Project administration.

Acknowledgments

Not applicable.

Ethics approval and consent to participate

All animal experiments were approved by the Institutional Animal Care and Use Committee.

Consent for publication

Not applicable.

Competing interests

Not applicable.

Funding

Not applicable.

Clinical Trial Number

Not applicable.

References

1. Moon Y., Shim M. K., Choi J., Yang S., Kim J., Yun W. S., Cho H., Park J. Y., Kim Y., Seong J. K. and Kim K., Anti-PD-L1 peptide-conjugated prodrug nanoparticles for targeted cancer immunotherapy combining PD-L1 blockade with immunogenic cell death, *Theranostics*, 2022, **12**(5).
2. Wang Q., Liang Q., Dou J., Zhou H., Zeng C., Pan H., Shen Y., Li Q., Liu Y., Leong D. T., Jiang W. and Wang Y., Breaking through the basement membrane barrier to improve nanotherapeutic delivery to tumours, *Nat Nanotechnol*, 2024, **19**(1).
3. Rui R., Zhou L. and He S., Cancer immunotherapies: advances and bottlenecks, *Frontiers in Immunology*, 2023, **14**.
4. Han X., Liu J., Zhang Y., Tse E., Yu Q., Lu Y., Ma Y. and Zheng L., Increasing the tumour targeting of antitumour drugs through anlotinib-mediated modulation of the extracellular matrix and the RhoA/ROCK signalling pathway, *J Pharm Anal*, 2024, **14**(8).
5. Lee C. K., Atibalentja D. F., Yao L. E., Park J., Kuruvilla S. and Felsher D. W., Anti-PD-L1 F(ab) Conjugated PEG-PLGA Nanoparticle Enhances Immune Checkpoint Therapy, *Nanotheranostics*, 2022, **6**(3): 243.
6. Akinleye A. and Rasool Z., Immune checkpoint inhibitors of PD-L1 as cancer therapeutics, *Journal of Hematology & Oncology*, 2019, **12**(1).
7. Yang Z., Gao D., Guo X., Jin L., Zheng J., Wang Y., Chen S., Zheng X., Zeng L., Guo M., Zhang X. and Tian Z., Fighting Immune Cold and Reprogramming Immunosuppressive Tumor Microenvironment with Red Blood Cell Membrane-Camouflaged Nanobullets, *ACS Nano*, 2020, **14**(12): 17442.
8. Yang Y., Lu Y., Zhang C., Guo Q., Zhang W., Wang T., Xia Z., Liu J., Cheng X., Xi T., Jiang F. and Zheng L., Phenazine derivatives attenuate the stemness of breast cancer cells through triggering ferroptosis, *Cell Mol Life Sci*, 2022, **79**(7).
9. Zhou Z., Mukundan N., Zhang J. A., Wu Y. T., Zhang Q., Wang D., Fang R. H., Gao W. and Zhang L., Macrophage-Mimicking Cellular Nanoparticles Scavenge Proinflammatory Cytokines in Specimens of Patients with Inflammatory Disorders, *Adv Sci (Weinh)*, 2024, **11**(31).
10. Li Y., Miao Y., Yang L., Zhao Y., Wu K., Lu Z., Hu Z. and Guo J., Recent Advances in the Development and Antimicrobial Applications of Metal-Phenolic Networks, *Adv Sci (Weinh)*, 2022, **9**(27).
11. Kesharwani P., Chadar R., Sheikh A., Rizg W. Y. and Safhi A. Y., CD44-Targeted Nanocarrier for Cancer Therapy, *Frontiers in Pharmacology*, 2022, **12**.
12. Li H., Wang M., Huang B., Zhu S. W., Zhou J. J., Chen D. R., Cui R., Zhang M. and Sun Z. J., Theranostic near-infrared-IIb emitting nanoprobes for promoting immunogenic radiotherapy and abscopal effects against cancer metastasis, *Nat Commun*, 2021, **12**(1).
13. DeOre B. J., Partyka P. P., Fan F. and Galie P. A., CD44 mediates shear stress mechanotransduction in an in vitro blood-brain barrier model through small GTPases RhoA and Rac1, *The FASEB Journal*, 2022, **36**(5).
14. Gong K., Lin J., Chen X., Duan Y., Zhang J., Yu J., Wang J., Sun R., Li J. and Duan Y., Thermosensitive gel-nano system against esophageal cancer via restoring p53 activity and boosting T-cell immunity, *Journal of Controlled Release*, 2024, **371**: 111.

15. Ji M., Zhan F., Qiu X., Liu H., Liu X., Bu P., Zhou B., Serda M. and Feng Q., Research Progress of Hydrogel Microneedles in Wound Management, *ACS Biomater Sci Eng*, 2024, **10**(8).
16. Lou J., Meyer C., Vitner E. B., Adu-Berchie K., Dacus M. T., Bovone G., Chen A., To T., Weitz D. A. and Mooney D. J., Surface-Functionalized Microgels as Artificial Antigen-Presenting Cells to Regulate Expansion of T Cells, *Advanced Materials*, 2024, **36**(31).
17. Tian Y., Xia L., Song X. and Chen Y., Dissolving Microneedles as In Situ Chemical Reaction Chambers: from Design Strategies to Versatile Biomedical Applications, *Advanced Functional Materials*, 2025, **35**(23).
18. Xiong G., Huang D., Lu L., Luo X., Wang Y., Liu S., Chen M., Yu S., Kappen M., You C., Lu S., Yu Y., Lu J. and Lin F., Near-Infrared-II Light Induced Mild Hyperthermia Activate Cisplatin-Artemisinin Nanoparticle for Enhanced Chemo/Chemodynamic Therapy and Immunotherapy, *Small Methods*, 2022, **6**(9).
19. Gong F., Xu J., Liu B., Yang N., Cheng L., Huang P., Wang C., Chen Q., Ni C. and Liu Z., Nanoscale CaH2 materials for synergistic hydrogen-immune cancer therapy, *Chem*, 2022, **8**(1): 268.
20. Zhou H., Zhang Y., Zhang R., Zhao M., Chen W., Liu Y., Jiang Y., Li Q., Miao Q. and Gao M., A Tumor-Microenvironment-Activatable Molecular Pro-Theranostic Agent for Photodynamic and Immunotherapy of Cancer, *Advanced Materials*, 2023, **35**(30).
21. Guo J., Cao Y., Wu Q. Y., Zhou Y. M., Cao Y. H. and Cen L. S., Implications of pH and Ionic Environment in Chronic Diabetic Wounds: An Overlooked Perspective, *Clin Cosmet Investig Dermatol*, 2024, **17**.
22. Wang Y., Yang T. and He Q., Strategies for engineering advanced nanomedicines for gas therapy of cancer, *Natl Sci Rev*, 2020, **7**(9).
23. Han X., Wang L., Li T., Zhang J., Zhang D., Li J., Xia Y., Liu Y. and Tan W., Beyond Blocking: Engineering RNAi-Mediated Targeted Immune Checkpoint Nanoblocker Enables T-Cell-Independent Cancer Treatment, *ACS Nano*, 2020, **14**(12): 17524.
24. Zhao Q., Hu J., Kong L., Jiang S., Tian X., Wang J., Hashizume R., Jia Z., Fowlkes N. W., Yan J., Xia X., Yi S. F., Dao L. H., Masopust D., Heimberger A. B. and Li S., FGL2-targeting T cells exhibit antitumor effects on glioblastoma and recruit tumor-specific brain-resident memory T cells, *Nat Commun*, 2023, **14**(1).
25. Zhou S., Zheng J., Zhai W. and Chen Y., Spatio-temporal heterogeneity in cancer evolution and tumor microenvironment of renal cell carcinoma with tumor thrombus, *Cancer Lett*, 2023, **572**.
26. Hou F., Guo Z., Ho M. T., Hui Y. and Zhao C. X., Particle-Based Artificial Antigen-Presenting Cell Systems for T Cell Activation in Adoptive T Cell Therapy, *ACS Nano*, 2024, **18**(12).
27. Sheehy T. L., Kwiatkowski A. J., Arora K., Kimmel B. R., Schulman J. A., Gibson-Corley K. N. and Wilson J. T., STING-Activating Polymer–Drug Conjugates for Cancer Immunotherapy, *ACS Central Science*, 2024, **10**(9): 1765.
28. Oliveira G. and Wu C. J., Dynamics and specificities of T cells in cancer immunotherapy, *Nature Reviews Cancer*, 2023, **23**(5): 295.

29. Amaria R. N., Reddy S. M., Tawbi H. A., Davies M. A., Ross M. I., Glitza I. C., Cormier J. N., Lewis C., Hwu W.-J., Hanna E., Diab A., Wong M. K., Royal R., Gross N., Weber R., Lai S. Y., Ehlers R., Blando J., Milton D. R., Woodman S., Kageyama R., Wells D. K., Hwu P., Patel S. P., Lucci A., Hessel A., Lee J. E., Gershenwald J., Simpson L., Burton E. M., Posada L., Haydu L., Wang L., Zhang S., Lazar A. J., Hudgens C. W., Gopalakrishnan V., Reuben A., Andrews M. C., Spencer C. N., Prieto V., Sharma P., Allison J., Tetzlaff M. T. and Wargo J. A., Neoadjuvant immune checkpoint blockade in high-risk resectable melanoma, *Nature Medicine*, 2018, **24**(11): 1649.
30. Voabil P., de Bruijn M., Roelofsen L. M., Hendriks S. H., Brokamp S., van den Braber M., Broeks A., Sanders J., Herzig P., Zippelius A., Blank C. U., Hartemink K. J., Monkhorst K., Haanen J. B. A. G., Schumacher T. N. and Thommen D. S., An ex vivo tumor fragment platform to dissect response to PD-1 blockade in cancer, *Nature Medicine*, 2021, **27**(7): 1250.
31. Waldman A. D., Fritz J. M. and Lenardo M. J., A guide to cancer immunotherapy: from T cell basic science to clinical practice, *Nature Reviews Immunology*, 2020, **20**(11): 651.
32. Yang Y., Qi J., Hu J., Zhou Y., Zheng J., Deng W., Inam M., Guo J., Xie Y., Li Y., Xu C., Deng W. and Chen W., Lovastatin/SN38 co-loaded liposomes amplified ICB therapeutic effect via remodeling the immunologically-cold colon tumor and synergized stimulation of cGAS-STING pathway, *Cancer Lett*, 2024, **588**.

Figures

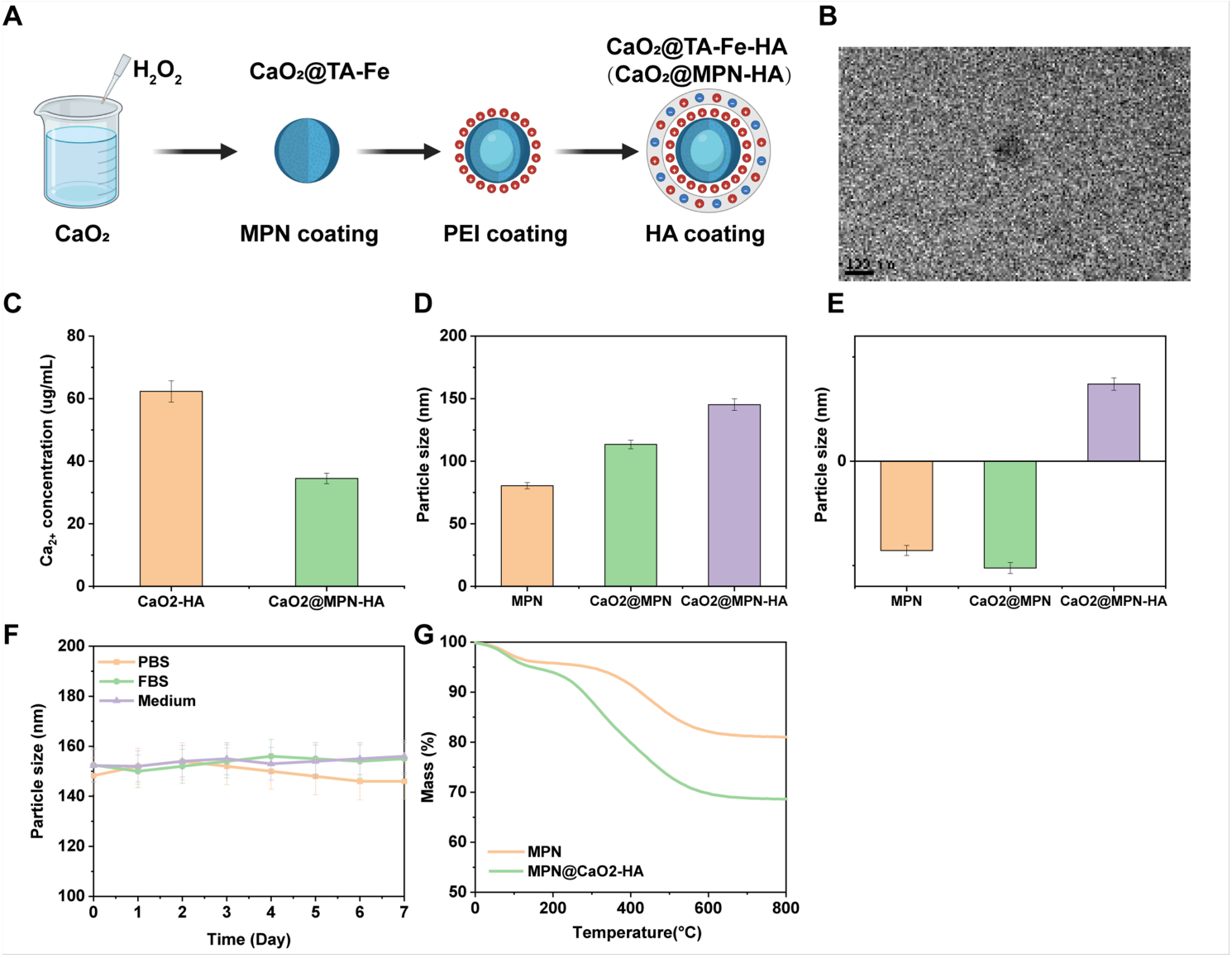

Figure 1

Preparation and Physicochemical Characterization of CaO_2@MPN-HA Nanoreactor.

A) Schematic illustration of the synthesis procedure for CaO_2@MPN-HA via stepwise layer-by-layer (LbL) assembly.

B) Representative transmission electron microscopy (TEM) images of CaO_2@MPN-HA nanoparticles, showing distinct core-shell structure (scale bar: 200 nm).

C) Ca^{2+} concentrations of pristine CaO_2 NPs (initial) and residual Ca^{2+} in the supernatant after encapsulation into MPN shell, determined by ICP-MS (n = 3 independent experiments, mean ± SD).

D) Hydrodynamic diameter of nanoparticles at each assembly stage (CaO_2, CaO_2@MPN, CaO_2@MPN-PEI, CaO_2@MPN-HA) measured by dynamic light scattering (DLS) in water.

E) Zeta potential of nanoparticles after each modification step, demonstrating successful charge reversal and final negative surface (n = 3 independent experiments, mean ± SD).

F) Colloidal stability of CaO_2@MPN-HA in different media (PBS, 10% FBS, and complete DMEM) over 7 days, monitored by changes in hydrodynamic diameter via DLS (n = 3 independent experiments, mean ± SD).

G) Thermogravimetric analysis (TGA) curves of bare MPN and CaO_2@MPN-HA under nitrogen atmosphere from 30 °C to 800 °C, confirming the successful loading of CaO_2 and organic components.

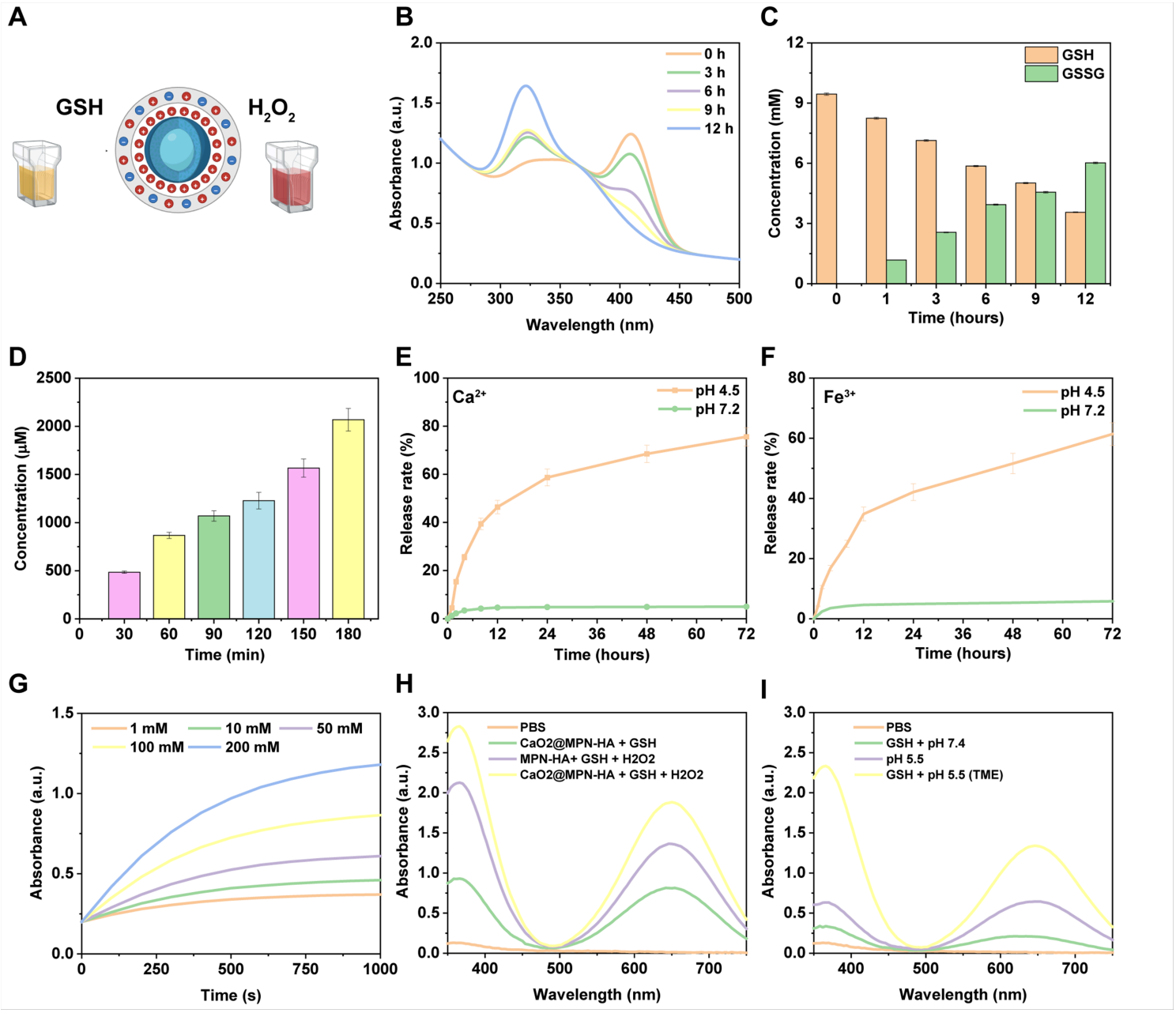

Figure 2

Tumor Microenvironment-Responsive Degradation and Cascade Catalytic Performance of CaO_2@MPN-HA Nanoreactor.

A) Schematic illustration of the TME-responsive cascade reactions, including GSH-mediated MPN disassembly, H_2O_2 self-supply, Fe^{3+}/Fe^{2+} cycling, and amplified ·OH generation.

B) Time-dependent UV-vis absorption spectra of CaO_2@MPN-HA after incubation with 10 mM GSH, showing gradual disassembly of the TA-Fe^{3+} coordination network.

C) Quantitative changes in reduced glutathione (GSH) and oxidized glutathione (GSSG) levels in the reaction system over time, measured by DTNB assay (n = 3 independent experiments, mean ± SD).

D) Time-dependent H_2O_2 generation from CaO_2@MPN-HA in pH 5.5 acetate buffer, detected by titanium sulfate colorimetry (n = 3 independent experiments, mean ± SD).

E) Cumulative Ca^{2+} release profiles from CaO_2@MPN-HA in buffers at pH 7.4 and pH 4.5 over 72 h, determined by ICP-MS (n = 3 independent experiments, mean ± SD).

F) Time-dependent Fe^{3+}/Fe^{2+} release profiles from CaO_2@MPN-HA in 10 mM GSH solutions at different pH values (pH 7.4 vs. pH 5.5), measured by ICP-MS (n = 3 independent experiments, mean ± SD).

G) Time-dependent absorbance changes at 492 nm of OPD oxidation catalyzed by CaO_2@MPN-HA in the presence of varying H_2O_2 concentrations, confirming Fenton-like catalytic activity.

H) UV-vis absorption spectra of TMB oxidation products (652 nm) in different treatment groups under simulated acidic GSH conditions (pH 5.5 + 10 mM GSH), demonstrating ·OH generation efficiency.

I) UV-vis absorption spectra of oxidized TMB after different treatments of CaO_2@MPN-HA, highlighting the critical role of both low pH and GSH in triggering maximal ·OH production.

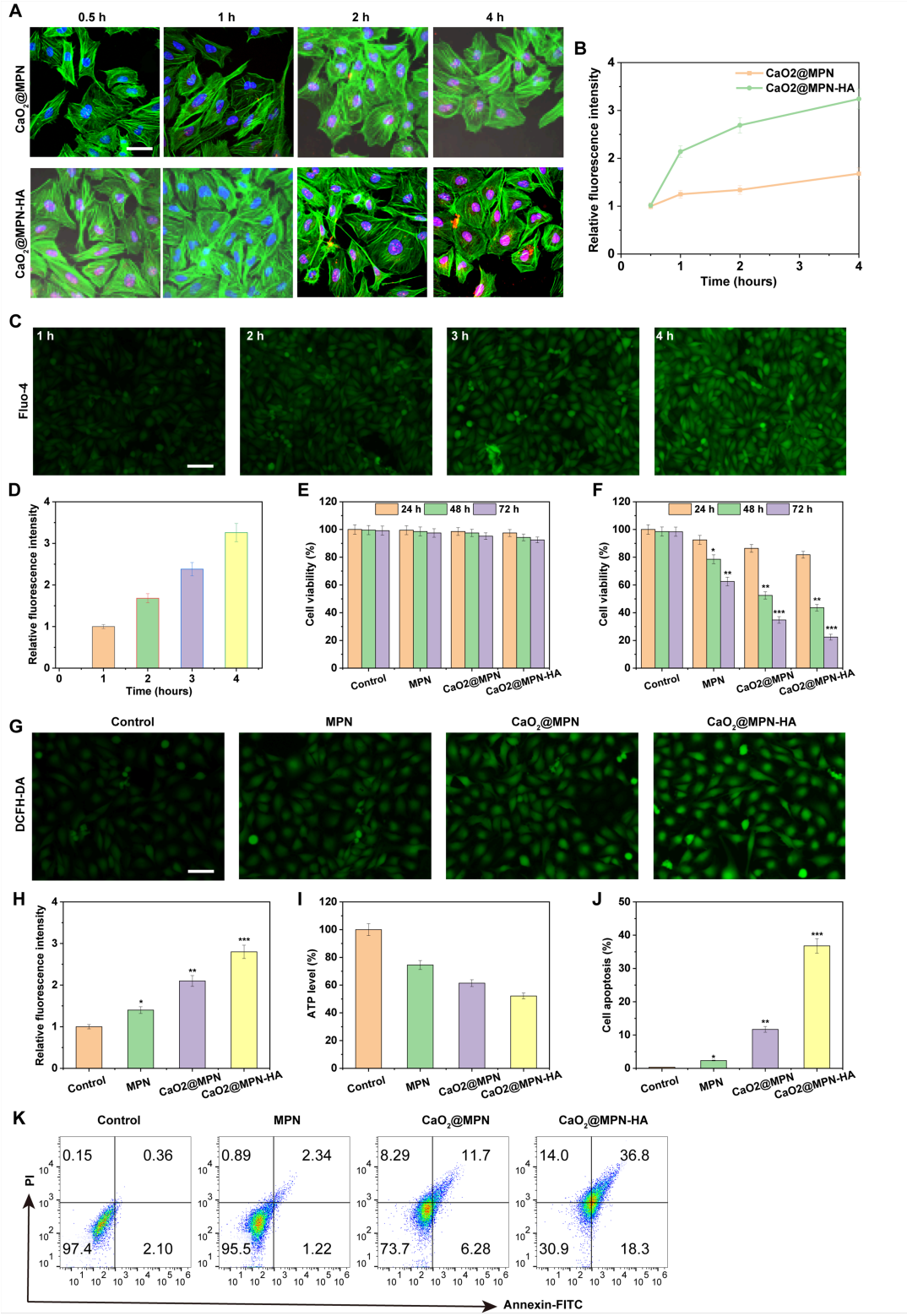

Figure 3

Cellular Uptake, Biosafety, and Synergistic Ferroptosis-Calcium Overload-Induced Cytotoxicity of CaO_2@MPN-HA *In Vitro*.

A) Representative confocal laser scanning microscopy (CLSM) images of TtT/GF cells after 4 h incubation with FITC-labeled CaO_2@MPN or CaO_2@MPN-HA (green: F-actin stained by Phalloidin-Alexa

Fluor 488; red: FITC-labeled nanoparticles; blue: DAPI-stained nuclei; scale bar: 20 μm).

B) Time-dependent quantitative analysis of intracellular FITC fluorescence intensity in TtT/GF cells treated with CaO_2@MPN or CaO_2@MPN-HA (0.5–4 h).

C) Representative CLSM images of intracellular Ca^{2+} levels in TtT/GF cells after 4 h treatment with different formulations, visualized using Fluo-4 AM probe (green fluorescence; scale bar: 50 μm).

D) Quantitative analysis of Fluo-4 AM fluorescence intensity reflecting intracellular Ca^{2+} concentration.

E) Cell viability of normal L929 fibroblasts after 48 h co-incubation with increasing concentrations of CaO_2@MPN-HA, assessed by CCK-8 assay.

F) Cell viability of TtT/GF tumor cells after 24, 48, and 72 h incubation with different formulations, determined by CCK-8 assay.

G) Representative fluorescence images of intracellular ROS generation in TtT/GF cells after 12 h treatment, detected by DCFH-DA probe (green fluorescence; scale bar: 100 μm).

H) Quantitative analysis of DCFH-DA fluorescence intensity.

I) Intracellular ATP levels in TtT/GF cells after 24 h treatment with different formulations, measured using an ATP assay kit.

J) Quantitative analysis of apoptosis/necrosis rates by Annexin V-FITC/PI staining and flow cytometry after 24 h treatment (Q2 + Q3: total apoptotic cells).

K) Representative flow cytometry dot plots of Annexin V-FITC/PI double staining for each treatment group.

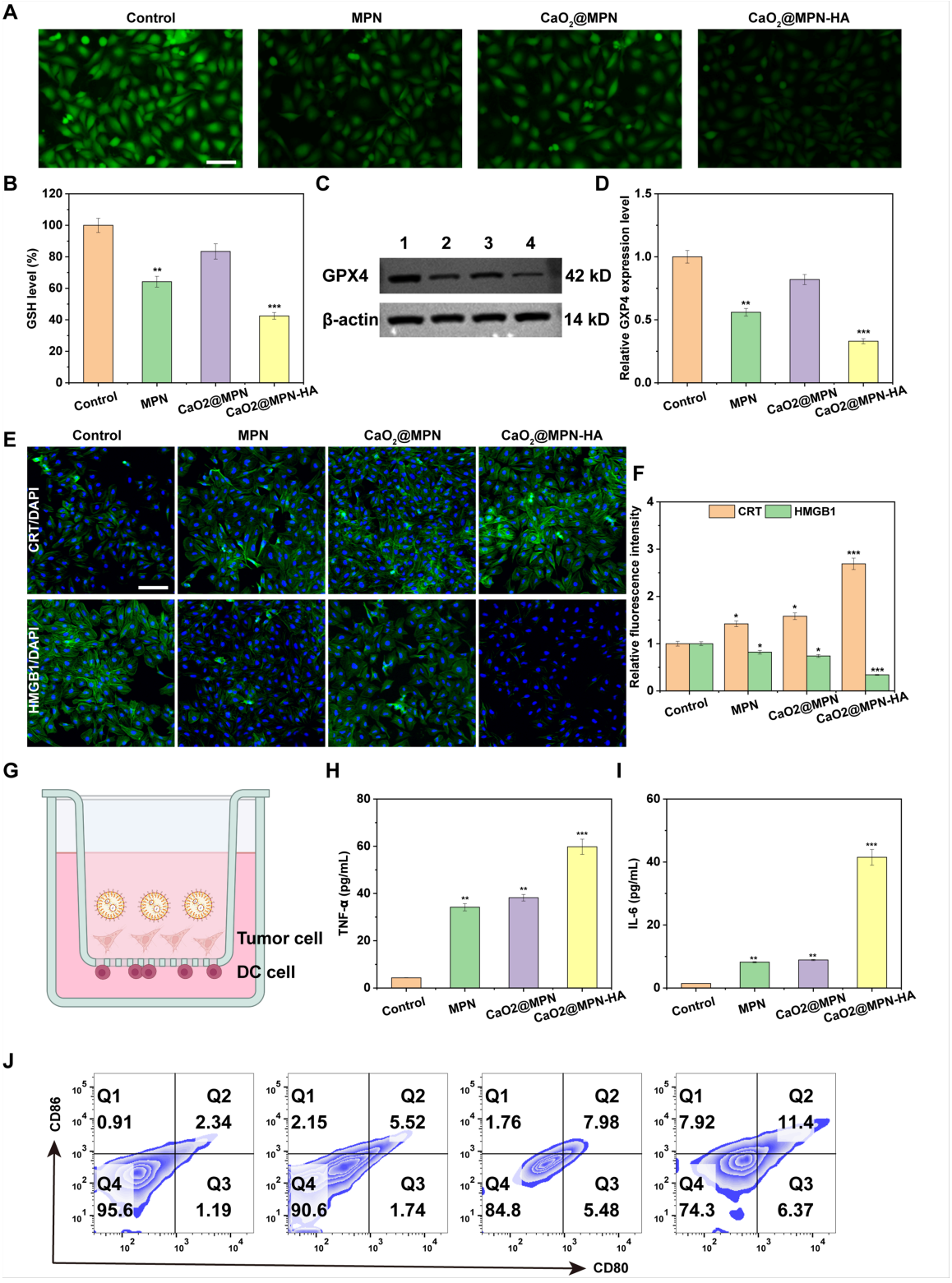

Figure 4

Mechanistic Validation of Ferroptosis and Induction of Immunogenic Cell Death (ICD) by CaO_2@MPN-HA.

A) Representative fluorescence images of intracellular GSH levels in TtT/GF cells after 24 h treatment with different formulations, visualized using ThiolTracker Violet dye (scale bar: 50 μm).

B) Quantitative analysis of relative intracellular GSH content measured by a commercial GSH assay kit.

C) Western blot analysis of GPX4 protein expression in TtT/GF cells after 24 h treatment with indicated formulations (β-actin as loading control).

D) qRT-PCR quantification of GPX4 mRNA levels in TtT/GF cells after 24 h treatment.

E) Representative immunofluorescence images showing surface exposure of calreticulin (CRT, red) and nuclear-to-cytoplasmic translocation/release of HMGB1 (green) in TtT/GF cells after 24 h treatment (nuclei stained with DAPI, blue; scale bar: 20 μm).

F) Quantitative analysis of CRT exposure (membrane fluorescence intensity) and HMGB1 release (nuclear depletion).

G) Schematic illustration of the Transwell co-culture system used to evaluate the immunostimulatory effect of drug-treated tumor cells on immature dendritic cells (DC2.4).

H) ELISA quantification of TNF-α secretion in the co-culture supernatant after 24 h.

I) ELISA quantification of IL-6 secretion in the co-culture supernatant after 24 h.

J) Flow cytometric analysis and quantification of mature dendritic cells ($CD11c^+CD80^+CD86^+$) after 24 h co-culture with drug-pretreated TtT/GF cells.

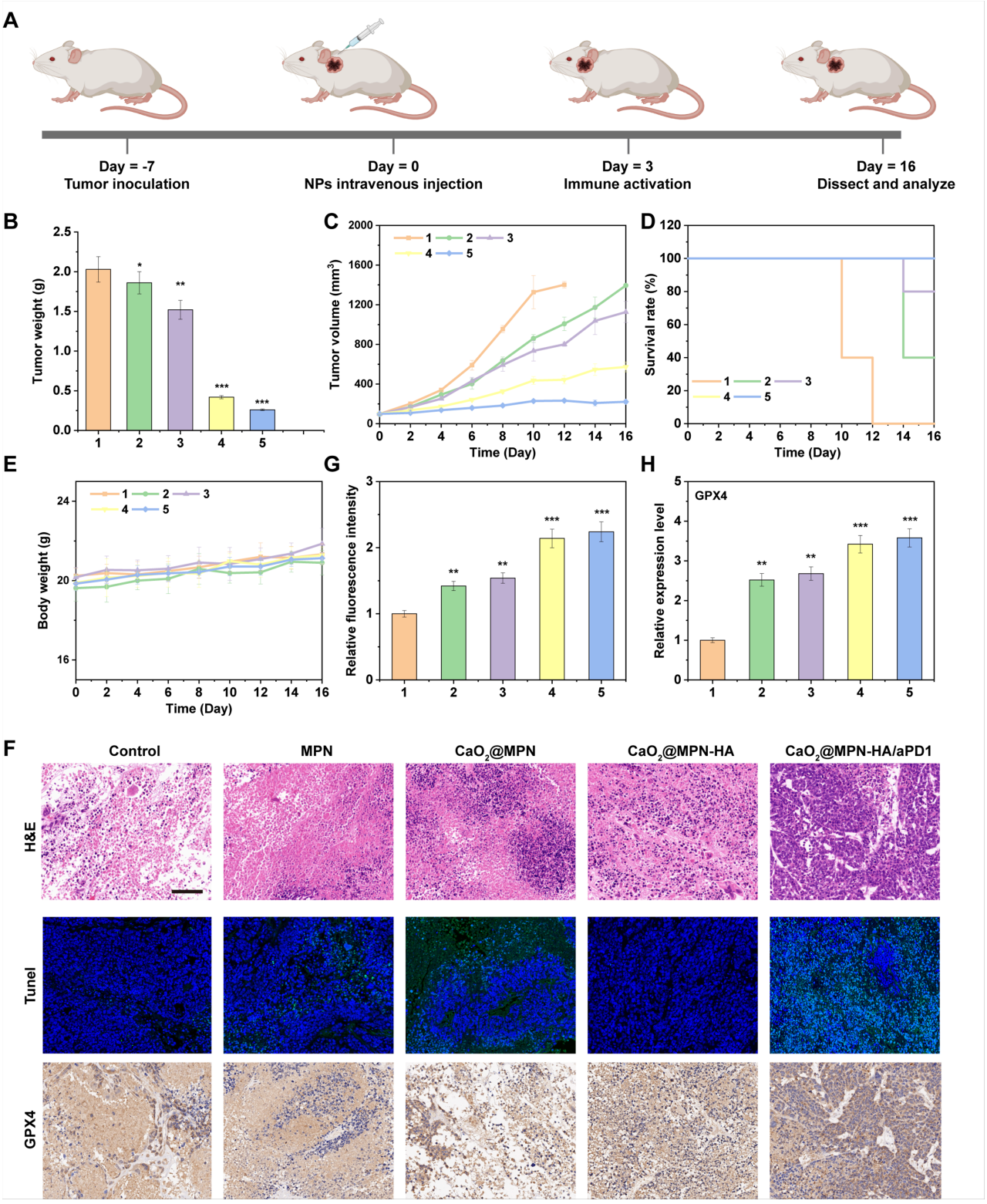

Figure 5

In Vivo Antitumor Efficacy of CaO_2@MPN-HA Combined with Anti-PD-1 Therapy in TtT/GF Thyroid Tumor-Bearing Mice.

A) Schematic illustration of the treatment schedule and proposed mechanism of synergistic ferroptosis-calcium overload therapy combined with immune checkpoint blockade.

B) Photographs of excised tumors and quantitative analysis of tumor weights from each group at the end of treatment.

C) Tumor growth curves of different treatment groups during the 16-day therapeutic period.

D) Kaplan–Meier survival curves of mice in each group over 16 days.

E) Body weight changes of mice in each group during the treatment period, indicating negligible systemic toxicity.

F) Representative H&E staining, TUNEL staining (green fluorescence), and GPX4 immunohistochemical staining (brown) of tumor sections collected at the end of treatment (scale bar: 100 μm).

G) Quantitative analysis of TUNEL-positive apoptotic cells in tumor tissues.

H) Quantitative analysis of GPX4 expression levels in tumor tissues by immunohistochemical scoring.

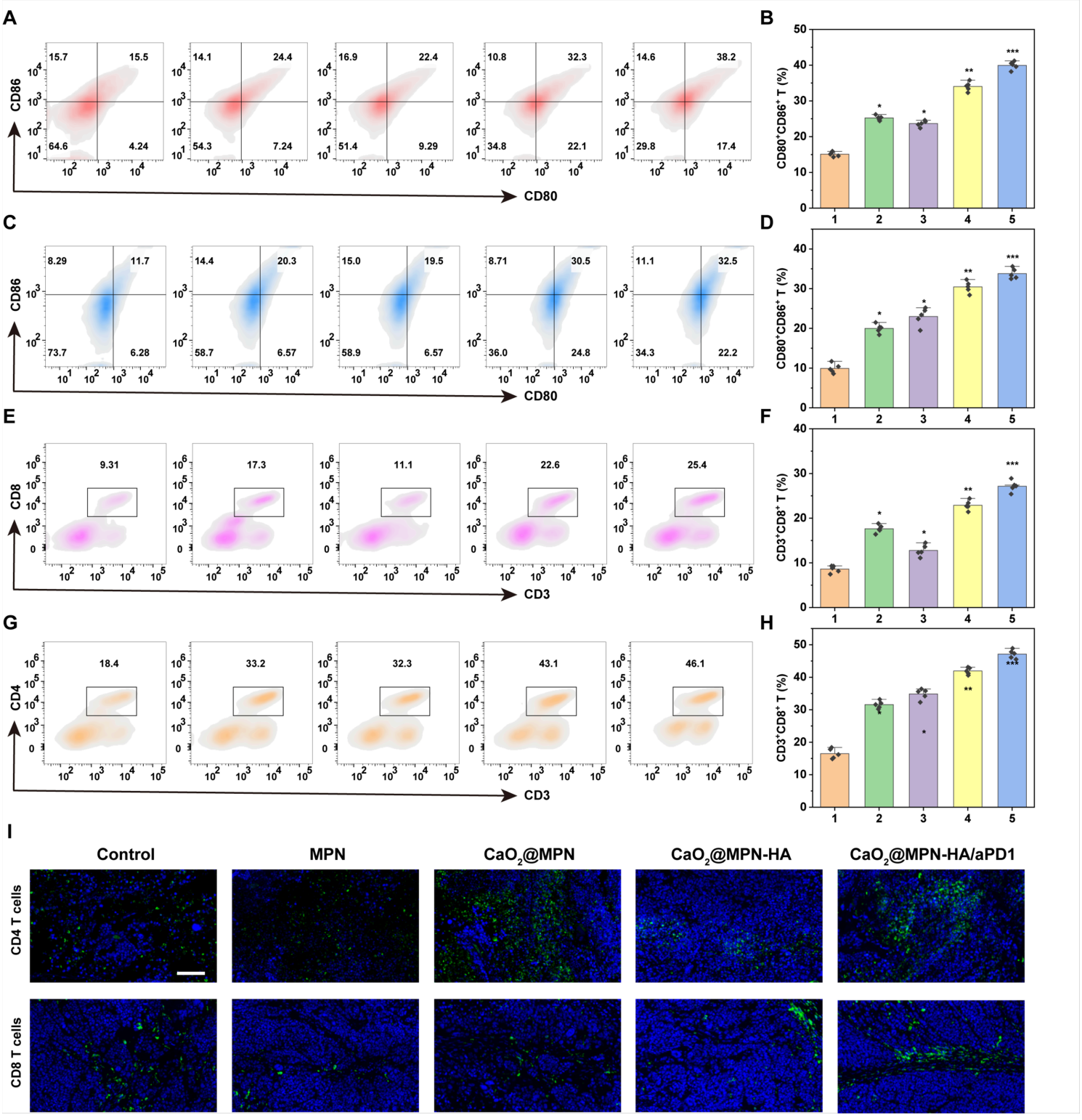

Figure 6

Systemic Immune Activation and Tumor Immune Microenvironment Remodeling Induced by CaO_2@MPN-HA plus Anti-PD-1 Therapy.

A) Representative flow cytometric plots and

B) Quantification of mature dendritic cells ($CD11c^+CD80^+CD86^+$) in spleens at the end of treatment.

C) Representative flow cytometric plots and

D) Quantification of mature dendritic cells ($CD11c^+CD80^+CD86^+$) in tumor-draining lymph nodes.

E) Representative flow cytometric plots and

F) Semiquantitative analysis of tumor-infiltrating cytotoxic T lymphocytes ($CD3^+CD8^+$) in distant tumors after different treatments.

G) Representative flow cytometric plots and

H) Semiquantitative analysis of tumor-infiltrating helper T cells ($CD3^+CD4^+$) in distant tumors after different treatments.

I) Representative immunofluorescence images of $CD4^+$ (green) and $CD8^+$ (red) T-cell infiltration in tumor sections from each group (nuclei counterstained with DAPI, blue; scale bar: 100 μm).

Supplementary Files

This is a list of supplementary files associated with this preprint. Click to download.

- Highlights.docx
- FigureAbstract.png
- FigureS6.tif
- FigureS2.tif
- FigureS1.tif
- FigureS5.tif
- FigureS3.tif
- FigureS4.tif